A PATH INTEGRAL MONTE CARLO (PIMC) METHOD BASED ON FEYNMAN-KAC FORMULA FOR ELECTRICAL IMPEDANCE TOMOGRAPHY*

CUIYANG DING †, YIJING ZHOU ‡, WEI CAI§, XUAN ZENG ¶, AND CHANHAO YAN ‖

Abstract. A path integral Monte Carlo method (PIMC) based on a Feynman-Kac formula for the Laplace equation with mixed boundary conditions is proposed to solve the forward problem of the electrical impedance tomography (EIT). The forward problem is an important part of iterative algorithms of the inverse EIT problem, and the proposed PIMC provides a local solution to find the potentials and currents on individual electrodes. Improved techniques are proposed to compute with better accuracy both the local time of reflecting Brownian motions (RBMs) and the Feynman-Kac formulas for mixed boundary problems of the Laplace equation. Accurate voltage-to-current maps on the electrodes of a model 3-D EIT problem with eight electrodes are obtained by solving a mixed boundary problem with the proposed PIMC method.

Key words. EIT, reflecting Brownian motion, boundary local time, Skorokhod problem, Feynman-Kac formula, walk-on-spheres, Laplace equation, mixed boundary problem, boundary element method.

AMS subject classifications. 60G60 62P30 78M50

1. Introduction.

Electrical Impedance Tomography (EIT) is often used as a non-invasive medical imaging technique to image the electrical properties such as the conductivity on a part of the body by surface electrode measurements. Its main advantage is the absence of exposure to radioactive materials, compared with other techniques such as X-rays. Applications of EIT include detection of breast cancer, blood clots, pulmonary emboli, etc.. Essentially, through only surface measurements, the internal electric conductivity is identified as an image inside the human body by solving an inverse problem. This is possible as the electric conductivity of malignant tumors, being a high-water-content tissue, is one order higher than that of surrounding normal (fat) tissues, allowing one to identify potential diseases and locations through the constructed image of the body [1]. EIT is also a useful tool in geophysics, environmental sciences, and nondestructive testing of materials. For example, it can be used to locate underground mineral deposits, detect leaks in underground storage tanks and monitor flows of injected fluids into the earth for the extraction or environmental cleaning. Moreover, EIT has also been used to find the corrosion or defects of construction and machinery parts [2] [1] without invasion or destructive testing.

For most of the applications, researchers are faced with the problem of finding out the conductivity inside an object with only partial boundary measurements [3]. This poses a great computational challenge as the conductivity inverse problem is nonlinear, unstable, and intrinsically ill-posed [2]. In theory, complete boundary measurements could determine the conductivity in the interior uniquely [4] [5]. However,

*Submitted to the SISC, June 18, 2020.

Funding: W. Cai was supported by US National Science Foundation (Grant No. DMS-1764187). X. Zeng and C. Yan were partly supported by National Natural Science Foundation of China (NSFC) research projects 61674042, 61974032, 61774045.

†State Key Laboratory of ASIC and System, Fudan University,Shanghai, China.

‡Department of Mathematics and Statistics, University of North Carolina at Charlotte, Charlotte, NC 28223, USA.

§Department of Mathematics Southern Methodist University, Dallas, TX75275.

¶State Key Laboratory of ASIC and System, Fudan University,Shanghai, China.

‖State Key Laboratory of ASIC and System, Fudan University,Shanghai, China.

in practice, only a limited number of electrodes and current patterns are available from measurements to reconstruct the conductivity. Various inversion algorithms have been proposed and fall into two categories, non-iterative and iterative methods. Non-iterative methods often assume that the conductivity is close to a constant. In [6], Calderón proved that a map between the conductivity function γ and a quadratic energy functional Q_γ is injective when γ is in a sufficiently small neighborhood of a constant function, and an approximation formula was given to reconstruct the conductivity. Among the iterative approaches, the back-projection method of Barber-Brown [7] gave a crude approximation to the conductivity increment $\delta\gamma$ based on the inverse of the generalized Radon transform, which works best for smooth $\delta\gamma$ or $\delta\gamma$ whose singularity is far from the boundary. For multiple electrode systems, Noser algorithm [1] minimizes the sum of squares error of the voltages on the electrodes by using one step of a regularized Newton's method. Also, various iterative methods are developed by minimizing different regularized least-squares functionals with a Tikhonov-type regularization [8][9] or a total variation regularization [10].

Solving the conductivity inverse problem with iterative algorithms requires a numerical solution of a forward problem at each iteration, therefore, the computation time accumulates fast for commonly used grid-based global methods such as the finite element method (FEM) or the boundary element method (BEM). In finding the conductivity profile to match the measured voltages over electrodes, a global solution of the potentials over the whole object is in fact not needed, therefore a global solution procedure during the forward problem incur unnecessary computational cost beyond the electrodes. With this in mind, in this paper, a local stochastic approach, a path integral Monte Carlo (PIMC) method using Feynman-Kac formula, will be proposed. Due to the nature of the Feynman-Kac formula which allows the potential solution at any single location such as those on the electrodes, we could dramatically reduce the storage and computing resources needed for each forward problem solution.

Recently, Maire and Simon [11] also proposed a probabilistic method of the voltage-to-current map using partially reflecting Brownian motions (with some given absorption and reflection probabilities on the electrodes). A walk-on-spheres (WOS) method was used to sample the paths of the Brownian motion in the interior while near the boundary, a finite difference discretization of the Laplace equation and the Robin boundary conditions were used to derive a probabilistic relation for the solution and then an integral equation with a corresponding transition probability kernel, whose solution was implemented with a Markov chain for a 2-D EIT problem [12]. In our approach, a pure probabilistic method for the voltage-to-current map uses a Feynman-Kac formula for the solution to the mixed boundary value problem, and directly simulates the reflecting Brownian motion paths as well as their local time on the boundary. It will avoid using finite difference meshing discretization, which could require a sophisticated mesh generation near the boundary of a complex and non-smooth domain. In our approach, the calculation of the boundary local time will be given careful considerations for the application of the Feynman-Kac representation. The voltages will be obtained numerically on the electrodes in a 3-D EIT problem, then the Neumann data, and henceforth the current on all electrodes.

The remainder of the paper is organized as follows. In Section 2, the forward problems of the EIT problem is introduced as well as a simplified model for the forward problem for our numerical experiments. Section 3 introduces reflecting Brownian motion (RBM), local time, and corresponding computational methods. Then, we propose the path integral Monte Carlo method based on Feynman-Kac formula for the mixed boundary value problem and an improved algorithm for computing the local

time of the RBM. In Section 4, a boundary element method (BEM) is described to generate reference solutions for validating the PIMC simulation. Comparison between the stochastic PIMC and the global BEM method, which shows the accuracy and advantages of the local and parallel PIMC method, is given in Section 5. Finally, conclusions and future work are discussed in Section 6.

2. Forward problems in EIT. In this section, we will first review the forward problem arising from EIT. The mathematic models for EIT have been developed and compared with the experimental measurement of voltages on electrodes for a given conductivity distribution, which is adjusted to fit the measurements. The existing models are continuum model, gap model, shunt model, and complete electrode model. Among all, the complete electrode model was shown to be capable of predicting the experimentally measured voltages to within 0.1 percent [13] and the existence and uniqueness of the model have also been proved.

Complete electrode model [1]. Let the domain of the object be denoted as Ω, embedded within which we assume there is an anomaly $\Omega_0 \subset \Omega$. The domain Ω is assumed to have a smooth boundary with a limited number of electrodes $E_i, i = 1, ..., L$ attached to $\partial\Omega$. The conductivity inside Ω is given by γ and the electric potential for the model will satisfy the following boundary value problem

$$\nabla \cdot \gamma \nabla u = 0, \quad \text{in } \Omega, \tag{1a}$$

$$\frac{1}{|E_l|} \int_{E_l} \gamma \frac{\partial u}{\partial n} dS = J_l, \quad l = 1, 2, ..., L, \tag{1b}$$

$$\gamma \frac{\partial u}{\partial n} = 0, \quad \text{off } \cup_{l=1}^{L} E_l, \tag{1c}$$

$$u + z_l \gamma \frac{\partial u}{\partial n} = U_l \quad \text{on } E_l, \quad l = 1, 2, ..., L, \tag{1d}$$

$$\sum_{l=1}^{L} |E_l| J_l = 0, \tag{1e}$$

$$u = u_0 \qquad \text{on } \partial\Omega_0. \tag{1f}$$

In (1f), we have prescribed a constant potential u_0 on the surface of the tumor anomaly, modelled as a perfect conductor. Actually, the constant u_0 is implicitly defined through the imposed electrode voltages and can be determined according to equation (1e) [11].

Equation (1a) can be derived from Maxwell equations by neglecting the time-dependence of the alternating current and assuming the current source inside the object to be zero [13]. Equation (1b) and (1c) indicate the knowledge of current density on and off the electrodes on the boundary, respectively. Equation (1d) takes account of the electrochemical effect by introducing z_l as the contact impedance or surface impedance, which quantitatively characterizes a thin, highly resistive layer at the contact between the electrode and the skin, which causes potential jumps according to the Ohms law. It should be noted that the regularity of potential u decreases as the contact impedance approaches zero [11], which becomes a huge hindrance to accurate numerical resolution as in practice usually good contacts with small contact impedance are used. Equation (1e) illustrates that the sum of current on all electrodes should be zero since there is no current source in the object. The current flowing into the object should equal that flows out. All these six equations constitute the boundary conditions of the domain $\Omega \backslash \Omega_0$. Within the complete electrode model, to obtain

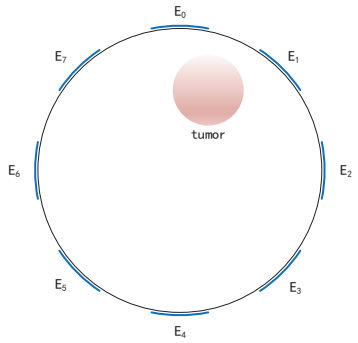

Fig. 1: Limited electrodes model on unit sphere with tumor

the voltage-to-current map is equivalent to solving the forward problem on the whole boundary given a known conductivity.

A model forward problem. In medical applications, a limited number of electrodes are attached to the human body to get surface measurements. We will illustrate our numerical method by modelling the problem inside a unit sphere. The sketch map of the model is shown in Fig. 1. Eight electrodes are superimposed on the boundary and the centers of the electrodes all lie on the $y-z$ plane evenly, each of width 0.2. The radius of the tumor equals 0.25.

Consider the conductivity equation with boundary conditions

$$\Delta u = 0 \quad \text{in } \Omega, \tag{2a}$$

$$\frac{\partial u}{\partial n} - cu = \phi_1(x) \quad \text{on } \Gamma_1 = \cup_{l=1}^{8} E_l, \tag{2b}$$

$$\frac{\partial u}{\partial n} = \phi_2(x) \quad \text{on } \Gamma_2 = \partial\Omega \backslash \Gamma_1, \tag{2c}$$

$$u = \phi_3(x) \quad \text{on } \Gamma_3 = \partial\Omega_0, \tag{2d}$$

where $c = -\frac{1}{\gamma z_l}$, and γ is the conductivity, the contact impedance of the electrode z_l is a constant between 0 and 1, $\phi_1(x) = \frac{1}{\gamma z_l} U_l$, and $\phi_3(x)$ is the constant potential on the tumor, and n is the outward unit normal. For our numerical simulation, we consider specifically the case that the conductivity γ is taken to be 1, the contact impedance $z_l = 0.5$, and the voltage on the electrodes U_l is assigned $\cos(4\theta)$ for $x = (r, \theta, \phi)$, $\phi_2(x) = 0$.

The forward problem is a Laplace problem with mixed boundary values. The surface boundaries on or off the electrodes are given Robin or Neumann conditions while the tumor has a Dirichlet boundary. In our previous work [14][15], we described a path integral Monte Carlo simulations to find potentials given Neumann or Robin boundaries through the WOS method (described in section 3.2). Here in this paper, a similar approach handling three kinds of boundary conditions simultaneously will be taken to find potentials on the electrode patches given mixed boundary conditions for the Laplace equation. After the potential approximations are found, the Neumann values are automatically known from the Robin boundary conditions on the electrode patches, and subsequently, the current on each electrode can be calculated according

to equation (1b). Therefore, the voltage-to-current map is obtained for the forward EIT problem.

3. A path integral Monte Carlo (PIMC) solution using Feynman-Kac formula. We will first review the Feynman-Kac formula for the mixed boundary value problem in (2a)-(2d), which lays the foundation of our PIMC approach.

3.1. Reflecting Brownian motion and boundary local time. Assume that D is a domain with a C^1 boundary in R^3 and a Skorokhod problem is defined as follows:

DEFINITION 3.1. *Let $f \in C([0,\infty), R^3)$, a continuous function from $[0,\infty]$ to R^3. A pair (ξ_t, L_t) is a solution to the Skorokhod equation $S(f;D)$ if*

1. *ξ is continuous in $\bar{D}$;*
2. *the local time $L(t)$ is a nondecreasing function which increases only when $\xi \in \partial D$, namely,*

$$L(t) = \int_0^t I_{\partial D}(\xi(s))L(ds); \tag{3}$$

3. *The Skorokhod equation holds:*

$$S(f;D): \qquad \xi(t) = f(t) - \frac{1}{2}\int_0^t n(\xi(s))L(ds), \tag{4}$$

where $n(x)$ denotes the outward unit normal vector at $x \in \partial D$.

The Skorokhod problem was first studied in [16] by A.V. Skorokhod in addressing the construction of paths for diffusion processes inside domains with boundaries, which experience the instantaneous reflection at the boundaries. Skorokhod presented the result in one dimension in the form of an Ito integral and Hsu [17] later extended the concept to d-dimensions ($d \geq 2$).

In general, the solvability of the Skorokhod problem is closely related to the smoothness of the domain D. For higher dimensions, the existence of (4) is guaranteed for C^1 domains while the uniqueness can be achieved for a C^2 domain by assuming the convexity for the domain [18]. Later, it was shown by Lions and Sznitman [19] that the constraints on D can be relaxed to some locally convex properties.

Suppose that $f(t)$ is a standard Brownian motion (SBM) path starting at $x \in \bar{D}$ and (X_t, L_t) is the solution to the Skorokhod problem $S(f;D)$, then X_t will be the standard reflecting Brownian motion (SRBM) on D starting at x. Because the transition probability density of the SRBM satisfies the same parabolic differential equation as that for a BM, a sample path of the SRBM can be simulated simply as that of the BM within the domain. However, the zero Neumann boundary condition for the density of SRBM implies that the path is pushed back at the boundary along the inward normal direction whenever it attempts to cross the boundary.

The boundary local time L_t is not an independent process but associated with SRBM X_t and defined by

$$L(t) \equiv \lim_{\epsilon \to 0} \frac{\int_0^t I_{D_\epsilon}(X_s)ds}{\epsilon}, \tag{5}$$

where D_ϵ is a strip region of width ϵ containing ∂D and $D_\epsilon \subset \overline{D}$. Here L_t is the local time of X_t, a notion invented by P. Lévy [20]. This limit exists both in L^2 and P^x-*a.s.* for any $x \in \overline{D}$.

It is obvious that L_t measures the amount of time that the standard reflecting Brownian motion X_t spends in a vanishing neighborhood of the boundary within the time period $[0, t]$. An interesting part of (5) is that the set $\{t \in R_+ : X_t \in \partial D\}$ has a zero Lebesgue measure while the sojourn time of the set is nontrivial [21]. This concept is not just a mathematical one but also has physical relevance in understanding the "crossover exponent" associated with "renewal rate" in modern renewal theory [22].

3.2. Simulation of RBM and calculation of local time. The WOS method was first proposed by Müller [23], which can solve the Dirichlet problem for the Laplace operator efficiently.

To illustrate the WOS method for the Dirichlet problem of Laplace equation, with Dirichlet boundary conditions ϕ, the solution can be rewritten in terms of a measure μ_D^x defined on the boundary ∂D,

$$u(x) = E^x(\phi(X_{\tau_D})) = \int_{\partial D} \phi(y) d\mu_D^x, \tag{6}$$

where μ_D^x is the harmonic measure defined by

$$\mu_D^x(F) = P^x\left\{X_{\tau_D} \in F\right\}, F \subset \partial D, x \in D. \tag{7}$$

It can be shown easily that the harmonic measure is related to the Green's function $g(y, x)$ for the domain with a homogeneous boundary condition [24], i.e.,

$$\begin{aligned} -\Delta g(x, y) &= \delta(x - y), \quad && x \in D, \\ g(x, y) &= 0, && x \in \partial D, \end{aligned}$$

as follows

$$p(\mathbf{x}, \mathbf{y}) = -\frac{\partial g(x, y)}{\partial n_y}. \tag{8}$$

If the starting point x of Brownian motion is at the center of a ball, the probability of the BM exiting a portion of the boundary of the ball will be proportional to the portion's area. Therefore, sampling a Brownian path by drawing balls within the domain can significantly reduce the path sampling time. To be specific, given a starting point x inside the domain D, we simply draw a ball of largest possible radius fully contained in D and then the next location of the Brownian path on the surface of the ball can be sampled, using a uniform distribution on the sphere, say at x_1. Treat x_1 as the new starting point, draw a second ball fully contained in D, make a jump from x_1 to x_2 on the surface of the second ball as before. Repeat this procedure until the path hits an absorption ϵ-shell of the domain (see Fig. 3(a)) [25]. When this happens, we assume that the path has hit the boundary ∂D (see Fig. 2(a) for an illustration).

Now we can define an estimator of (6) by

$$u(x) \approx \frac{1}{N} \sum_{i=1}^{N} u(x_i), \tag{9}$$

where N is the number of Brownian paths sampled and x_i is the first hitting point of each path on the boundary. To speed up the WOS process, the maximum possible size of the sphere for each step would allow faster first hitting on the boundary, see Fig. 2(b).

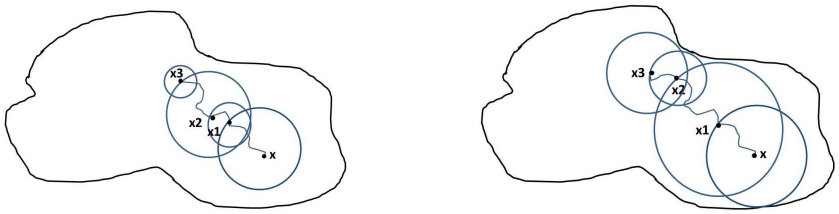

(a) WOS within the domain

(b) WOS (with a maximal step size for each jump) within the domain

Fig. 2: Walk-on-spheres method

For the reflecting boundary, we will construct a strip region around the boundary (see Fig. 3(a)) and allow the process X_t to move according to the law of BM continuously. Before the path enters the strip region, the radius of WOS is chosen to be of a maximum possible size within the distance to the boundary. Once the particle is in the strip region, the radius of the WOS sphere is then fixed at a constant Δx (or $2\Delta x$, see Fig. 3(b)). With this approach, according to the definition (5), the local time may be interpreted as

$$dL(t) \approx \frac{\int_{t_{j-1}}^{t_j} I_{D_\epsilon}(X_s)ds}{\epsilon}, \tag{10}$$

which is

$$dL(t) \approx \frac{\int_{t_{j-1}}^{t_j} I_{D_\epsilon}(X_s)ds}{\epsilon} = (n_{t_j} - n_{t_{j-1}})\frac{(\Delta x)^2}{3\epsilon}, \tag{11}$$

given a prefixed radius Δx inside the $\epsilon-$strip region and n_{t_j} is the cumulative steps that path stays within the ϵ-region from the beginning until time t_j (see Remark below for definition). Notice that only those steps where the path of X_t stays in the ϵ-region will contribute to n_{t_j} while the SRBM may stay out of the ϵ-region at other steps. More details can be found in [14].

Remark I. Occupation time of SRBM X_t in the numerator of (10) was calculated in terms of that of BM sampled by the walks on spheres. Notice here that within the ϵ-region, the radius of the WOS may be Δx or $2\Delta x$, which implies that the corresponding elapsed time of one step for local time could be $(\Delta x)^2/3$ or $(2\Delta x)^2/3$. The latter is four times bigger than the former. But if we absorb the factor 4 into n_t, (11) will still hold. In practical implementation, we treat n_t as a vector of entries of increasing value, the increment of each component of n_t over the previous one after each step of WOS will be 0, 1 or 4, corresponding to the scenarios that X_t is out of the ϵ-region, in the ϵ-region while sampled on the sphere of a radius Δx, or in the ϵ-region while sampled on the sphere of a radius $2\Delta x$, respectively. The increase of the radius from Δx to $2\Delta x$ is to sample the collision of the path of the boundary more efficiently.

3.3. PIMC based on Feynamn-Kac formula and accuracy of local time. We consider the mixed boundary value problem in the domain $\Omega\backslash\Omega_0$ to the mixed

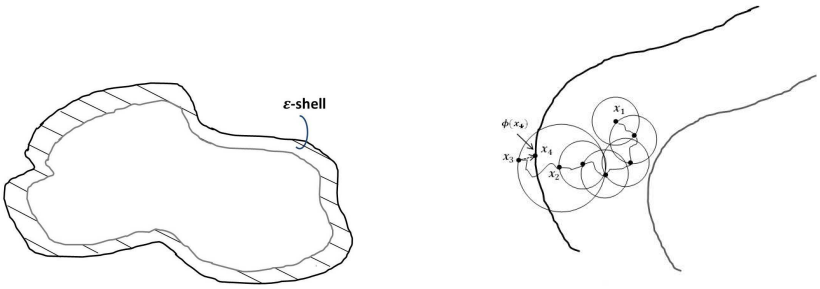

(a) A ϵ-region for a bounded domain in R^3

(b) WOS in the ϵ-region

Fig. 3: Walk on Spheres near the boundary

problem (2a)-(2d). A probabilistic solution for the mixed boundary value problem is given by a Feynman-Kac formula [26] [27]

$$u_{Mix}(x) = \frac{1}{2}E^x\left\{\int_0^\infty \hat{e_c}(t)\phi_1(X_t)dL(t)\right\} + \frac{1}{2}E^x\left\{\int_0^\infty \phi_2(X_t)dL(t)\right\} + E^x(\phi_3(X_{\tau_{\Gamma_3}})). \tag{12}$$

where X_t is the standard reflecting Brownian motion, $L(t)$ is the corresponding local time and the Feynman-Kac functional $\hat{e_c}(t) := e^{\frac{1}{2}\int_0^t c(X_t)dL(t)}$, τ_{Γ_3} is the first time a Brownian path originating from $\Omega\backslash\Omega_0$ hits the boundary of $\partial\Omega_0 = \Gamma_3$. It is noted that the integral for the Robin data $\phi_1(X_t)$ (as well as $\hat{e_c}(t)$) has an extra factor $\frac{1}{2}$ compared with the original formula in [26] due to different definition of the local time used in this paper and [26] (as also reflected the additional 1/2 in the Skorokhod equation (4) in comparison with equation (1.2) in [26]).

The Feynman-Kac formula provides a local solution procedure to solve the partial differential equations through stochastic processes.

The numerical approximation to (12) will be

$$\tilde{u}_{Mix}(x) = \frac{1}{2}E^x\left\{\int_0^T e^{\frac{1}{2}\int_0^t c(X_s)dL(s)}\phi_1(X_t)dL(t)\right\} + \frac{1}{2}E^x\left\{\int_0^T \phi_2(X_t)dL(t)\right\} + E^x(\phi_3(X_{\tau_{\Gamma_3}})), \tag{13}$$

or

$$\tilde{u}_{Mix}(x) = \frac{1}{2}E^x\left\{\sum_{j=0}^{NP} e^{\frac{1}{2}\int_0^{t_j} c(X_s)dL(s)}\phi_1(X_{t_j})dL(t_j)\right\} + \frac{1}{2}E^x\left\{\sum_{j=0}^{NP} \phi_2(X_{t_j})dL(t_j)\right\} + E^x(\phi_3(X_{\tau_{\Gamma_3}})). \tag{14}$$

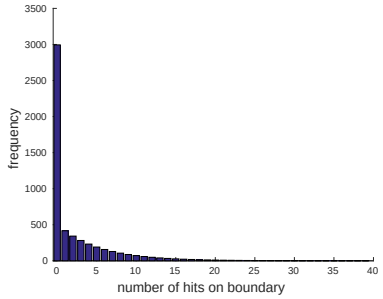

(a) The occurrence frequency of different numbers of hits on boundary between an entry into and an exit out of the ϵ-region. Numerical parameters: Spherical domain with a Neumann data, $NP = 8e4$,$\Delta x = 5e-4$, $\epsilon = 2.5\Delta x$. 56.06% of cases found with no collision on the boundary.

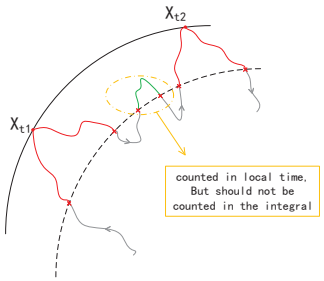

(b) A schematic diagram of typical scenery of a path hitting the reflecting boundary.

Fig. 4: The scenery of the path hitting the reflecting boundary.

Equivalently,

$$\tilde{u}_{Mix}(x) = \frac{1}{2}E^x\left\{\sum_{j:X_{t_j}\in E}^{NP} e^{\frac{1}{2}\int_0^{t_j} c(X_s)dL(s)}\phi_1(X_{t_j})dL(t_j)\right\} + \frac{1}{2}E^x\left\{\sum_{j:X_{t_j}\in\Gamma_2}^{NP}\phi_2(X_{t_j})dL(t_j)\right\} + E^x(\phi_3(X_{\tau_{\Gamma_3}})), \tag{15}$$

where all the expectation E^x is taken as the average of all paths starting from x.

In our previous work [14] and [15], the terms involving local time increment inside the integrand of (15) are approximated by

$$\phi_i(X_{t_j})dL(t_j) \approx \phi_i(X_{t_j})(n_{t_j} - n_{t_{j-1}})\frac{(\Delta x)^2}{3\epsilon}, i = 1, 2 \tag{16}$$

where t_{j-1} and t_j are two consecutive collisions a path has with the boundary of Ω and the vector n_{t_j} records the vector of WOS steps inside the ϵ-region until time t_j (please see **Remark I** for the the enumeration convention of the WOS steps) and $n_{t_j} - n_{t_{j-1}}$ will be the increment of the vector of the local time between these two collisions. On a closer examination of the path collision history inside the ϵ-region, there are many cases where paths enter the ϵ-region and come out without colliding with the boundary as in Fig. 4(a). Fig. 4(b) is a schematic diagram depicting the situation where the path collides with the boundary twice and is reflected. In the calculation method in (16), Part ②, Part ③ and Part ④ are considered as the local time increment corresponding to collision point X_{t_2}, which counts mistakenly the increment caused by the path entering the ϵ-region but not hitting the boundary between the two collision points (Part ③).

To avoid this over-count in the definition of local time increment, we will keep track of each entry (t_{in}) and exit time (t_{out}) of the path into the ϵ-region, instead,

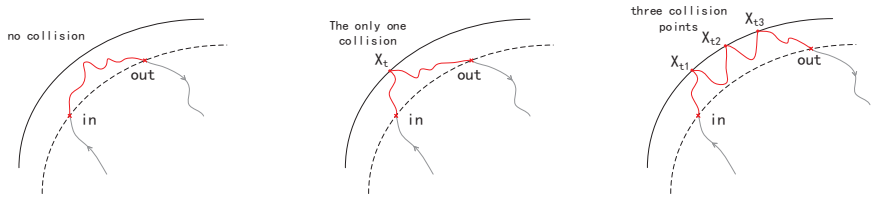

(a) number of hits = 0. (b) number of hits = 1. (c) number of hits = m.

Fig. 5: Three situations of the path walking in the ϵ-region.

and define the local time increment for each possible collision within this time period. Namely, To compute δn_{t_j} corresponding to the collision point X_{t_j}, we record the increment of the vector of the WOS steps $n_{j,out} - n_{j,in}$ between one entry into and one exit out of the ϵ-region by a path during this period X_{t_j} takes, and also the number of collisions m_j at the boundary during the same time period, and then set

$$\delta n_{t_j} = \begin{cases} \frac{n_{j,out}-n_{j,in}}{m_j}, \text{if } m_j > 0 \\ 0, \qquad \text{if } m_j = 0 \end{cases}, \tag{17}$$

which should give $\delta n_{t_j} = 0$ in Fig. 5(a), $\delta n_{t_j} = n_{j,out} - n_{j,in}$ in Fig. 5(b), and $\delta n_{t_j} = \frac{n_{j,out}-n_{j,in}}{m_j}$ for each of the three collisions at t_j's in Fig. 5(c).

Then, we can discretize the time integral over $[t_{in}, t_{out}]$ as follows,

$$\begin{aligned} \int_{t_{in}}^{t_{out}} \hat{e_c}(t)\phi_1(X_t)dL(t) &\approx \sum_{\text{collusion at } t_j \in [t_{in},t_{out}]} \hat{e_c}(t_j)\phi_1(X_{t_j})\delta n_{t_j}\frac{(\Delta x)^2}{3\epsilon}, \\ \int_{t_{in}}^{t_{out}} \phi_2(X_t)dL(t) &\approx \sum_{\text{collusion at } t_j \in [t_{in},t_{out}]} \phi_2(X_{t_j})\delta n_{t_j}\frac{(\Delta x)^2}{3\epsilon}, \end{aligned} \tag{18}$$

where a middle point rule at $t = t_j$ was used to evaluate the integrand $\phi_i(X_t)$. Meanwhile, the Feynman-Kac functional $\hat{e_c}(t_j)$ above can be simply approximated by

$$\hat{e_c}(t_j) = \sum_{\text{all } [t_{in},t_{out}] \text{ before } t_j} \frac{1}{2}\int_{t_{in}}^{t_{out}} c(X_s)dL(s) \approx exp[\sum_{\text{collision at } t_k \le t_j} \frac{1}{2}c(X_{t_k})\delta n_{t_k}\frac{(\Delta x)^2}{3\epsilon}]. \tag{19}$$

So, finally, we have the new approximation

$$\begin{aligned} \tilde{u}_{Mix}(x) = &\frac{1}{2}E^x\left\{\sum_{j'=0}^{NP} e^{\frac{1}{2}\sum_{k=0}^{j} c(X_{t_k})\delta n_{t_k}\frac{(\Delta x)^2}{3\epsilon}}\phi_1(X_{t_j})\delta n_{t_j}\frac{(\Delta x)^2}{3\epsilon}\right\} \\ &+ \frac{1}{2}E^x\left\{\sum_{j'=0}^{NP}\phi_2(X_{t_j})\delta n_{t_j}\frac{(\Delta x)^2}{3\epsilon}\right\} + E^x(\phi_3(X_{\tau_{\Gamma_3}})), \end{aligned} \tag{20}$$

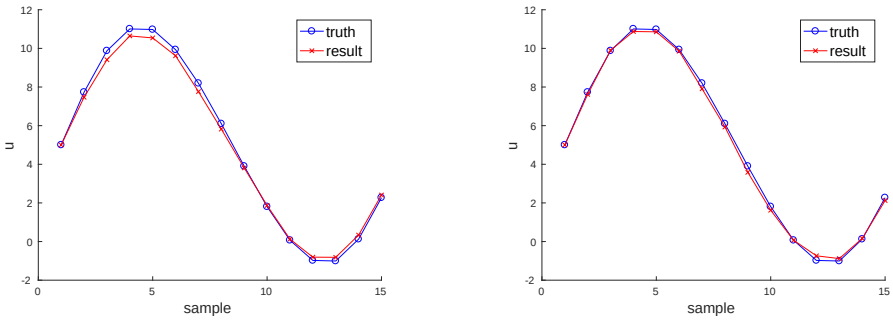

(a) The original method; $N = 2e5$, $NP = 3e4$, $\Delta x = 5e-4$, $\epsilon = 2.5\Delta x$; average error = 3.96% (5.13% reported in the original text).

(b) The modified method; $N = 2e5$, $NP = 3e4$, $\Delta x = 5e-4$, $\epsilon = 1.4\Delta x$; average error = 1.38%.

Fig. 6: The PIMC results for potential on 15 points inside a sphere for a Neumann problem of the Laplace equation with an exact solution $u = \sin 3x \sin 4y e^{5z} + 5$, calculated by two different ways of local time: (left) local time by (16), (right) local time by (18).

where j' denotes each step of the path and j denotes the steps where the path hits the boundary (Robin or Neumann).

The new approach in computing the local time has greatly improved the accuracy of the PIMC. Compared with about 4% error achieved by the previous method, the new approach can reduce the error to 1%. Here, we give one example to illustrate the improvement in a test case in [14]. The numerical results calculated by two different ways of computing the local time increment at each collision on boundary are shown in Fig. 6. Using the new calculation method for the local time, numerical experiments show that the result is optimal when the jump distance in the reflecting boundary region Δx is set to be 5e-4 and the width of the ϵ-region $\epsilon = 1.4\Delta x$. These two values are used in all of our numerical experiments, including the Neumann problem, the Robin problem and the mixed boundary value problem, and all the experiments achieve good results. When the number of Monte Carlo simulations N is large enough, as the path length parameter NP increase, the simulation result converges to the true reference value with an error of 1%. We also note that with the previous computational method for the local time, the optimal choice for the width of the ϵ-region was found also by numerical experiments to be $\epsilon = 2.5\Delta x$.

Remark II. We emphasize that in the process of simulating the SRBM, three situations should be considered, which are shown in Fig. 5(a)-5(c). The local time generated when the path travels in the ϵ-region but does not collide with the boundary as indicated in Fig. 5(a) will not contribute to the integral involving the local time increment and boundary data at collision sites. When the path hits the reflecting boundary once during walking in the ϵ-region, the local time increment corresponding to the collision point equals the local time generated by the path walking in the ϵ-region. In all other cases where the path collides with the boundary multiple times after entering the area as shown in Fig. 5(c), the generated local time increment is evenly distributed to these several collision points. Therefore, in the calculation of

the path integral, it is worth noting that not all the local time generated during the path walk is needed in the computation of the boundary data integrals.

3.4. Algorithm details for the PIMC method for mixed boundary problems. Using the simulation of RBM and the modified statistical method, Algorithm 1 gives a pseudo-code for the numerical realization of the proposed path integral Monte Carlo method for mixed boundary problems.

For RBM in a domain given mixed boundary conditions, the random walk path is reflected on the Neumann or Robin boundary and is absorbed on the Dirichlet boundary. Especially in the forward EIT problem, it is necessary to consider the distances to sphere and tumor, respectively. When the path enters the respective strip region of the absorbing or reflecting boundary, the corresponding operation needs to be completed, that is, the path is reflected on $\partial\Omega$ or absorbed on $\partial\Omega_0$.

In the Algorithm 1, code in line 4 - line 14 illustrates the transition from the current point to a new point according to the current position. If the point is in the strip region around the reflecting boundary, the radius of the jump will be changed to Δx or $2\Delta x$ and corresponding local time increment will be recorded(line 7 - line 12). When the next point is outside the reflecting boundary, a forced drawing back operation needs to be done(line 15 - line 18). Once the point hits the boundary, the value and the type of boundary need to be recorded for the follow-up data processing(line 19 - line 27). If the number of transition counts up to NP and the path has not been absorbed, the path will be truncated compulsively. The path integral is calculated with formula (20) after each path ends.

In order to obtain accurate mathematical expectations, a large number of paths should be sampled and the potential approximation of the starting point is the average of these path integrals.

4. A deterministic solution with the boundary element method. To provide reference solutions to the path integral MC method proposed above, we will present a deterministic method based on boundary element method for the mixed boundary value problem (2a)-(2d).

4.1. Graded boundary mesh. For boundary element method for the simplified forward model, a specially designed boundary mesh must be established over electrodes. Boundary mesh on $\partial\Omega$ is constructed on the electrode patches and off-electrodes, respectively, as shown in Fig. 7. For our implementation, GMSH is used to generate an unstructured 2D mesh consisting of flat triangles given the size of each triangle on off-electrode patch, and a simple mapping will fit the grid to the boundary. On the electrode patches, the meshes are structured in such a way that mesh points are located at the intersection of divisions along the longitude and altitude to gives a body-fitted mesh and the mapping from the elemental triangle to the curved ones can be found in [28]. On the surface of the tumor $\partial\Omega_0$, meshes are structured in a similar way by divisions along the latitude and longitude of $\partial\Omega_0$. A global boundary integral equation can then be set up with the meshes on $\partial\Omega$ and $\partial\Omega_0$.

A close look at the boundary conditions in (2b) and (2c) reveals discontinuities in potential at the rims of all the electrodes. Therefore, it is natural to enlarge the meshing area for the electrode E_i so that we have more control over the mesh size for better accuracy. Assume the enlarged radius to be $r_e = 0.3$. Because of the discontinuities, we consider a graded mesh on the enlarged surface by introducing a layered mesh structure, as Fig. 8 illustrates. There are four layers: the first ranges from center to r_1, second from r_1 to r, third from r to r_2 and fourth from r_2 to

Algorithm 1 PIMC method for mixed boundary problems

Input: The information of the domain and the boundary, the number of Monte Carlo simulations N, the length of each path NP, the starting point X_0, the width of the ϵ-region of the reflecting boundary $\epsilon_{reflecting}$, the step size of the WOS inside the ϵ-region near the reflecting boundary Δx, and the width of the absorption ϵ-shell of the absorbing boundary $\epsilon_{absorbing}$.

Output: An approximation of $u(X_0)$.

Initialization: $L[NP]$, $v[NP]$ and $type[NP]$.

for $pathcount = 1 : N$ **do**
  $X = X_0$
  for $stepcount = 1 : NP$ **do**
    R_r = the distance from X to the reflecting boundary;
    R_a = the distance from X to the absorbing boundary;
    $R_{max} = min\{R_r, R_a\}$;
    if $0 < R_r \leq \Delta x$ **then**
      $R_{max} = 2\Delta x$, $L[stepcount] = 4$;
    end if
    if $\Delta x < R_r < \epsilon_{reflecting}$ or $R_r = 0$ **then**
      $R_{max} = \Delta x$, $L[stepcount] = 1$;
    end if
    Make a ball with the current point as the center and R_{max} as the radius;
    Take a new point X_t on the ball with uniform probability;
    if X_t is outside the reflecting boundary **then**
      Find a point X_c on the reflecting boundary which is closest to X_t;
      $X_t = X_c$;
    end if
    if X_t is on the reflecting boundary **then**
      $v[stepcount] = \varphi(X_c)$;
      $type[stepcount]$ records type of boundary(Neumann: 2, Robin: 3);
    end if
    R_a = the distance from X_t to the absorbing boundary;
    if $R_a \leq \epsilon_{absorbing}$ **then**
      $v[stepcount] = \varphi(X_t)$;
      $type[stepcount] = 1$;
      End the walk path;
    else $X = X_t$;
    end if
  end for
  Calculate the path integral with L, v and $type$ using formula (20).
end for
return $u(X_0)$ = the average of the integrals of all paths.

r_e. A dense mesh will be used around the rim ($r = 0.2$) of the electrode, namely, both the 2nd layer and 3rd layer should have a decreasing mesh size towards $r = 0.2$. Furthermore, a graded mesh also discretizes the first layer while an evenly distributed mesh is used on the fourth layer. And m_1, m_2, m_3 and m_4 are the number of divisions along the altitude in each layer, respectively. Here we take $m_1 = 15, m_2 = 12, m_3 = 12$

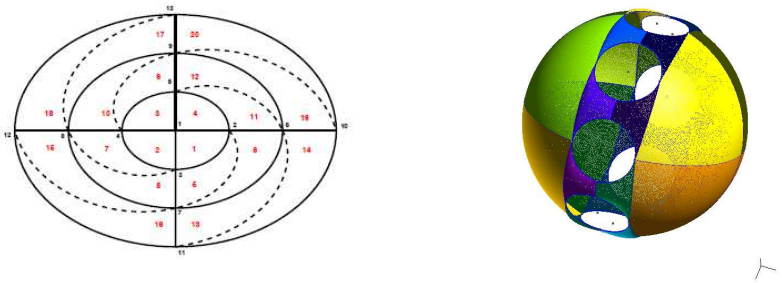

(a) Curved triangular mesh on an electrode

(b) Curved triangular mesh off-electrode patches

Fig. 7: Curved triangular meshes for EIT problem.

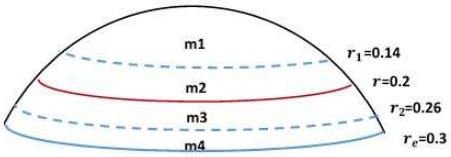

Fig. 8: Graded mesh on electrode patches.

and $m_4 = 7$. The mesh size can be calculated through $dx \cdot \alpha^i, i = 0, ..., m_j - 1(\alpha = 3/4, j = 1, 2, 3, 4)$. The number of divisions along the longitude is the same for each layer, i.e. $n = 60$. There are 55300 mesh points and 109588 flat triangle elements on off-electrode patch as shown in Fig.7(b) and the numbers of divisions along the latitude and longitude of Ω_0 are 50 and 60, respectively.

4.2. Boundary integral equation. By using the second Green's identity, we have the following relation for any fixed $x \in \Omega \backslash \Omega_0$,

(21)
$$\int_\Gamma (u(y)\Delta G(x,y) - G(x,y)\Delta u(y))\, dy = \int_\Gamma \left(\frac{\partial G(x,y)}{\partial n_y} u(y) - \int_\Gamma G(x,y) \frac{\partial u(y)}{\partial n_y} \right) ds_y,$$

where $\Gamma = \Gamma_1 \cup \Gamma_2 \cup \Gamma_3$ and $G(x, y)$ is the fundamental solution of the Laplace operator, namely,

(22)
$$G(x,y) = \frac{1}{4\pi} \frac{1}{|x-y|}.$$

As $x \to \Gamma$ from $\Omega \backslash \Omega_0$, we obtain for $x \in \Gamma$

$$\begin{aligned}\frac{1}{2}u(x) &= \int_{\Gamma} G(x,y)\frac{\partial u(y)}{\partial n_y}ds_y - \int_{\Gamma}\frac{\partial G(x,y)}{\partial n_y}u(y)ds_y,\\ &= \int_{\partial\Omega\bigcup\partial\Omega_0} G(x,y)\frac{\partial u(y)}{\partial n_y}ds_y - \int_{\partial\Omega\bigcup\partial\Omega_0}\frac{\partial G(x,y)}{\partial n_y}u(y)ds_y \end{aligned} \tag{23}$$

If we substitute the boundary conditions on the three kinds of boundaries (2b)-(2d) into the equation, when $x \in \Gamma_1 \cup \Gamma_2$, i.e. $\partial\Omega$, the equation becomes

$$\begin{aligned}\frac{1}{2}u(x) &= \int_{\Gamma_1} G(x,y)(\phi_1(y)+cu(y))ds_y - \int_{\Gamma_1}\frac{\partial G(x,y)}{\partial n_y}u(y)ds_y + \int_{\Gamma_2} G(x,y)\phi_2(y)ds_y\\ &- \int_{\Gamma_2}\frac{\partial G(x,y)}{\partial n_y}u(y)ds_y + \int_{\Gamma_3} G(x,y)\frac{\partial u(y)}{\partial n_y}ds_y - \int_{\Gamma_3}\frac{\partial G(x,y)}{\partial n_y}\phi_3(y)ds_y,\end{aligned} \tag{24a}$$

or when $x \in \Gamma_3$, i.e. $\partial\Omega_0$, the equation becomes

$$\begin{aligned}\frac{\phi_3(x)}{2} &= \int_{\Gamma_1} G(x,y)(\phi_1(y)+cu(y))ds_y - \int_{\Gamma_1}\frac{\partial G(x,y)}{\partial n_y}u(y)ds_y + \int_{\Gamma_2} G(x,y)\phi_2(y)ds_y\\ &- \int_{\Gamma_2}\frac{\partial G(x,y)}{\partial n_y}u(y)ds_y + \int_{\Gamma_3} G(x,y)\frac{\partial u(y)}{\partial n_y}ds_y - \int_{\Gamma_3}\frac{\partial G(x,y)}{\partial n_y}\phi_3(y)ds_y.\end{aligned} \tag{24b}$$

After taking $u(x)$ on $\partial\Omega$ and $\frac{\partial u(x)}{\partial n_x}$ on $\partial\Omega_0$ as the unknowns, substituting the parameters and rearranging the equation, we obtain a global boundary integral equation for the forward EIT problem

$$\begin{aligned}&\frac{1}{2}u(x) + \int_{\Gamma_1}(\frac{\partial G(x,y)}{\partial n_y} - G(x,y)c)u(y)ds_y + \int_{\Gamma_2}\frac{\partial G(x,y)}{\partial n_y}u(y)ds_y\\ &- \int_{\Gamma_3} G(x,y)\frac{\partial u(y)}{\partial n_y}ds_y\end{aligned}$$

$$= \int_{\Gamma_1} G(x,y)\phi_1(y)ds_y - u_0\int_{\Gamma_3}\frac{\partial G(x,y)}{\partial n_y}ds_y, \quad x \in \partial\Omega \tag{25a}$$

$$\int_{\Gamma_1}(\frac{\partial G(x,y)}{\partial n_y} - G(x,y)c)u(y)ds_y + \int_{\Gamma_2}\frac{\partial G(x,y)}{\partial n_y}u(y)ds_y - \int_{\Gamma_3} G(x,y)\frac{\partial u(y)}{\partial n_y}ds_y$$

$$= \int_{\Gamma_1} G(x,y)\phi_1(y)ds_y - (\frac{1}{2} + \int_{\Gamma_3}\frac{\partial G(x,y)}{\partial n_y}ds_y)u_0, \quad x \in \partial\Omega_0. \tag{25b}$$

Equation (25a) is the equation for $x \in \partial\Omega$ and (25b) is the equation for $x \in \partial\Omega_0$. With the different meshes on $\partial\Omega$ and $\partial\Omega_0$, letting x loop over all the mesh points, we have a linear system for solving $u(x)$ on $\partial\Omega$ and $\frac{\partial u(x)}{\partial n_x}$ on $\partial\Omega_0$ and the equation dimension equals the number of the mesh points on $\partial\Omega\bigcup\partial\Omega_0$. The potential inside the domain can be computed through

$$u(x) = \int_{\Gamma} G(x,y)\frac{\partial u(y)}{\partial n_y}ds_y - \int_{\Gamma}\frac{\partial G(x,y)}{\partial n_y}u(y)ds_y, \tag{26}$$

Table 1: The influence of the tumor position on electrode potential

tumor			*potential at* $(0,0,1)$		
position	*radius*	*potential on tumor*	*no tumor*	*with tumor*	*relative difference*
$(0.5,0,0)$		-0.01957		0.233339	0.121%
$(0,0,0)$		-0.01962		0.233342	0.122%
$(0,0,0.25)$		-0.01940		0.232866	-0.082%
$(0,0,0.4)$	0.25	-0.01700	0.233058	0.230048	-1.292%
$(0,0,0.5)$		-0.01225		0.223350	-4.165%
$(0,0,0.6)$		-0.00222		0.202139	-13.267%
$(0,0,0.7)$		0.01806		0.120227	-48.413%
$(0.169,0.197,0.541)$		-0.01850		0.223928	-3.917%
$(0.183,0.213,0.586)$		-0.01775		0.220476	-5.399%

where $\frac{\partial u(y)}{\partial n_y}$, the Neumann values on Γ_1, are automatically known once the reference potentials are found on the electrode patches from the Robin conditions (2b).

For comparison, we also need to calculate the solution of the case without the tumor Ω_0. The spherical domain is empty and $\Gamma = \partial\Omega = \Gamma_1 \cup \Gamma_2$. The boundary integral equation is built for mesh points on $\partial\Omega$ and the derivation is similar to the process above. The adjusted equation below can be obtained.

$$\begin{aligned} &\frac{1}{2}u(x) + \int_{\Gamma_1} (\frac{\partial G(x,y)}{\partial n_y} - G(x,y)c)u(y)ds_y + \int_{\Gamma_2} \frac{\partial G(x,y)}{\partial n_y} u(y)ds_y \\ &= \int_{\Gamma_1} G(x,y)\phi_1(y)ds_y, \quad x \in \Gamma_1 \cup \Gamma_2. \end{aligned} \tag{27}$$

The equation dimension equals the number of all the mesh points on $\partial\Omega$. From the equation, we can work out $u(x)$ on $\partial\Omega$ and obtain the global potential distribution though (26), again.

Table 2: Center potential and current density on each electrode for case 1 by BEM

electrode	*no tumor*		*with tumor*		*relative difference*	
	center potential	*current density*	*center potential*	*current density*	*center potential*	*current density*
E_0	0.233058	1.344907	0.202139	1.395272	-13.267%	3.745%
E_1	-0.274693	-1.403436	-0.271830	-1.409190	-1.042%	0.410%
E_2	0.247192	1.462005	0.250982	1.453928	1.533%	-0.552%
E_3	-0.274693	-1.403436	-0.271031	-1.411251	-1.333%	0.557%
E_4	0.233058	1.344907	0.236666	1.337196	1.548%	-0.573%
E_5	-0.274693	-1.403436	-0.271031	-1.411251	-1.333%	0.557%
E_6	0.247192	1.462005	0.250983	1.453928	1.534%	-0.552%
E_7	-0.274693	-1.403436	-0.271830	-1.409190	-1.042%	0.410%
overall	-	0.000010	-	-0.000070	-	-

4.3. Tumor locations and electrode potential and current computed by BEM. In order to confirm the numerical results of proposed PIMC method, the BEM discussed above will be used to produce a reference solution for the forward EIT problem. As the effect of the tumor on the electrodes depends on the location of the

Table 3: Center potential and current density on each electrode for case 2 by BEM

electrode	*no tumor*		*with tumor*		*relative difference*	
	center potential	*current density*	*center potential*	*current density*	*center potential*	*current density*
E_0	0.233058	1.344907	0.220476	1.369742	-5.399%	1.847%
E_1	-0.274693	-1.403436	-0.264733	-1.423535	-3.626%	1.432%
E_2	0.247192	1.462005	0.250304	1.455330	1.259%	-0.457%
E_3	-0.274693	-1.403436	-0.273258	-1.406504	-0.522%	0.219%
E_4	0.233058	1.344907	0.233775	1.343370	0.308%	-0.114%
E_5	-0.274693	-1.403436	-0.274522	-1.403797	-0.062%	0.026%
E_6	0.247192	1.462005	0.246626	1.463222	-0.229%	0.083%
E_7	-0.274693	-1.403436	-0.277192	-1.398048	0.910%	-0.384%
overall	-	0.000010	-	-0.000027	-	-

tumor. We exam first the potential at the center of the north pole electrode (0,0,1) for our study. The result in Table 1 shows that the tumor has a bigger effect on the closest electrode. If the distance is large, the difference between the case with and without the tumor may be too small to be distinguished in experiments.

In the following numerical experiments, we will set the position of the tumor at **case 1:** (0,0,0.6) and **case 2:** (0.183,0.213,0.586). In these two cases, the influence of the tumor on each electrode in terms of center potential and current density of (1b) is shown in Table 2 and Table 3. Compared with the results in case 2, the electrode currents in case 1 show symmetric patterns with respect to the z-axis when the tumor is at (0,0,0.6), consistent with the system setting. Meanwhile, the tumor can be found to have the most impact on the electrode E_0 among the eight electrodes. In case 1, the relative difference of current density over E_0 is 3.745% and the relative difference of the potential at (0,0,1) is -13.267%. While in case 2, when the tumor is close to both E_0 and E_1, the difference of the electrode currents on E_0 and E_1 is more obvious than that on other electrodes. The potentials over the north pole electrode with or without a tumor in these two cases calculated by BEM illustrate a visible difference especially in the central region (refer to the contour Fig. 11 and Fig. 12).

5. PMIC solution for EIT and computational cost. The PIMC method proposed in Section 3.4 will be used to compute the potential and current density over electrodes for the situations with or without tumor presence in the media and two cases of tumor locations as in Section 4.3 will be considered.

Path number N and path length NP in PIMC. The number of Monte Carlo simulations N is set to be $2e5$ for all the mesh points on the electrodes. The length of path NP is $5e5$ for the case without the tumor and $4e5$ for the cases with the tumor. A discussion about the value of NP is presented below. The step size of the WOS inside the ϵ-region near the boundary Δx is set to be $5e-4$, the width of the ϵ-region of the reflecting boundary $\epsilon_{\text{reflecting}} = 1.4\Delta x$, and the width of the absorption ϵ-shell of the absorbing boundary (i.e., boundary of the tumor) $\epsilon_{\text{absorbing}} = 1e-5$. We expect that for large enough N, as NP increases, the simulation result will approach the true (reference) value. To illustrate this, we show the relation between the result and NP in Fig. 9 and Fig. 10.

In our experiments, the criteria for path length truncation NP is that the results stabilize. If the tumor is included inside, it is easy to decide when to truncate. Due

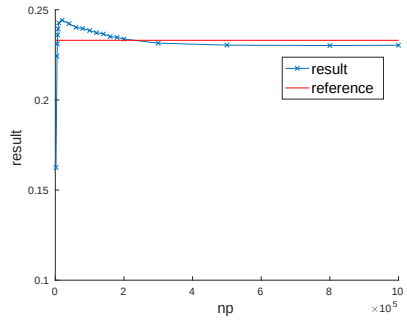

(a) potential of the center of E_0 (without tumor).

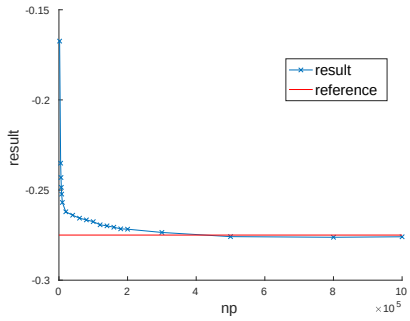

(b) potential of the center of E_1 (without tumor).

Fig. 9: Convergence of potential in terms of NP in the case without tumor (The red horizontal line is the reference value by BEM).

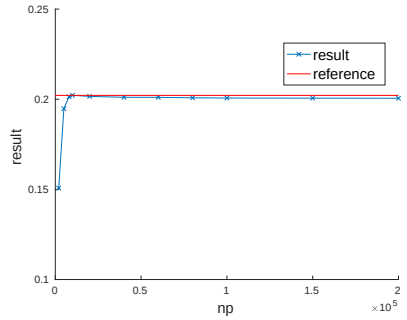

(a) potential of the center of E_0 (with tumor).

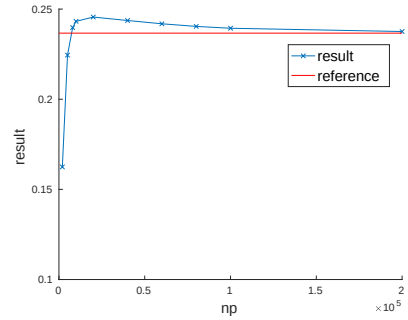

(b) potential of the center of E_4 (with tumor).

Fig. 10: Convergence of potential in terms of NP in case 1 with tumor (The red horizontal line is the reference value by BEM).

to the absorbing nature of the tumor, all paths will eventually be absorbed by the tumor in theory. The path truncation standard is that over 99% of the path have been absorbed. When NP is set to be $4e5$, the rate of absorption of the paths starting from the point furthest from the tumor $(0, 0, -1)$ reaches 99.6%, more than enough to meet this requirement. However, if there is no tumor inside the object, the paths will keep walking inside the domain. Since the contribution of the Neumann part is zero, the forward EIT problem without the tumor can be regarded as a Robin problem. For the Robin problem, due to the existence of the factor $\hat{e_c}(t)$ inside the integrand, when the length of the path is long enough, the impact of the subsequent collisions on the integral can be ignored. Our numerical experiments found that $\int_0^t dL(t_j)$ (j denotes the steps where the path hits the boundary) is proportional to NP with a proportional constant of $1.2 * \frac{(\Delta x)^2}{3\epsilon}$. Therefore, it can be estimated from this relationship how large NP should be when the factor reaches one-thousandth or even smaller. In addition,

Table 4: The potentials at electrode center by BEM and PIMC (case 1)

electrode	*no tumor*			*with tumor*		
	BEM	*PIMC*	*relative error*	*BEM*	*PIMC*	*relative error*
E_0	0.233058	0.230452	-1.118%	0.202139	0.201335	-0.398%
E_1	-0.274693	-0.274986	0.107%	-0.271830	-0.271401	-0.158%
E_2	0.247192	0.246814	-0.153%	0.250982	0.252035	0.419%
E_3	-0.274693	-0.277815	1.137%	-0.271031	-0.272039	0.372%
E_4	0.233058	0.231721	-0.574%	0.236666	0.237154	0.206%
E_5	-0.274693	-0.274991	0.108%	-0.271031	-0.270064	-0.209%
E_6	0.247192	0.245973	-0.493%	0.250983	0.250753	-0.092%
E_7	-0.274693	-0.275193	0.182%	-0.271830	-0.272877	0.385%

Table 5: The current density on the electrodes by BEM and PIMC (case 1)

electrode	*no tumor*			*with tumor*		
	BEM	*PIMC*	*relative error*	*BEM*	*PIMC*	*relative error*
E_0	1.344907	1.348172	0.243%	1.395272	1.392903	-0.170%
E_1	-1.403436	-1.399544	-0.277%	-1.409190	-1.413753	0.324%
E_2	1.462005	1.451656	-0.708%	1.453928	1.457768	0.264%
E_3	-1.403436	-1.398606	-0.344%	-1.411251	-1.408849	-0.170%
E_4	1.344907	1.348858	0.294%	1.337196	1.335640	-0.116%
E_5	-1.403436	-1.409004	0.397%	-1.411251	-1.414051	0.198%
E_6	1.462005	1.455570	-0.440%	1.453928	1.454157	0.016%
E_7	-1.403436	-1.392665	-0.767%	-1.409190	-1.403815	-0.381%
overall	0.000010	0.004437	-	-0.000070	0.000000	-

considering that the ratio of Robin boundary area to Neumann boundary area in this problem is 1:11.35, the value of NP needs to be about 12 times the value for an all Robin problem. Obviously, this is a rough heuristic estimate and can only serve as a guide. If a more accurate truncation is needed, dynamic monitoring of the factor $\hat{e_c}(t)$ can be used. Calculating the value of the factor in real-time when paths are walking can make the truncation more accurate, but also incur certain computational cost.

During the random walk simulation, the specific value of the constant potential on the tumor u_0 is unknown. However, because almost all paths end on the tumor, in fact the third term in formula (20) is approximately equal to u_0. Therefore, the potential approximation can be written as a sum $u = u' + u_0$, where u' is the sum of the first two terms in formula (20). According to equation (1b) and equation (1e), we can get an expression of total current (zero) on the electrodes, from which the value of constant u_0 can be determined by

$$\sum_{l=1}^{8} \int_{E_l} (\phi_1(x) + c(u' + u_0)) dS = 0. \tag{28}$$

Potentials and current density on electrodes by PIMC method. The center potentials and current density on the eight electrodes obtained by two methods are shown in Table 4 - Table 7, compared with the BEM result. As seen from the tables, the relative errors of the potentials between the PIMC results and the reference values remain at a low 1% level, which validates the PIMC method. Fig. 11 and Fig. 12 show potentials over the north pole electrode with or without the tumor calculated

Table 6: The potentials at electrode center by BEM and PIMC (case 2)

electrode	*with tumor*		
	BEM	*PIMC*	*relative error*
E_0	0.220476	0.221932	0.660%
E_1	-0.264733	-0.263901	-0.314%
E_2	0.250304	0.252272	0.786%
E_3	-0.273258	-0.276384	1.144%
E_4	0.233775	0.235597	0.779%
E_5	-0.274522	-0.278139	1.318%
E_6	0.246626	0.245983	-0.261%
E_7	-0.277192	-0.280570	1.219%

Table 7: The current density on the electrodes by BEM and PIMC (case 2)

electrode	*with tumor*		
	BEM	*PIMC*	*relative error*
E_0	1.369742	1.363416	-0.462%
E_1	-1.423535	-1.428400	0.342%
E_2	1.455330	1.445816	-0.654%
E_3	-1.406504	-1.407319	0.058%
E_4	1.343370	1.341553	-0.135%
E_5	-1.403797	-1.395027	-0.625%
E_6	1.463222	1.468290	0.346%
E_7	-1.398048	-1.388329	-0.695%
overall	-0.000027	0.000000	-

by PIMC. The potentials along the equator on E_0 and E_1 in case 1 and case 2 are presented in Fig. 13. It can be seen that the results in case 2 are slightly less symmetric than that in case 1 due to the position of the tumor. With the numerical approximations of potentials on the boundary, the Neumann values can be found from (2b), and the current from (1b) by evaluating the integral of the Neumann data with Gauss quadratures, thus, the voltage-to-current map can been achieved.

Computational cost of PIMC vs BEM. In terms of computational time cost, if the global problem is calculated, the average time of BEM per mesh point seems to be less. In the case without tumor, it takes 35,687s for BEM to build and solve an equation with 77,388 mesh points, of which 12,968 points are on the electrodes, while the PIMC method requires about 1,000s to calculate the potential at one point. In the cases with tumor, it takes about 75,000s for BEM to build and solve an equation with 80,330 mesh points, of which 12,968 points are on the electrodes, while the PIMC method requires 100s-300s to calculate the potential at one point (depends on the distance from the tumor). 60 threads are used in parallel to build the boundary integral equation in BEM and simulate the random walk of the paths in the PIMC method. Since our standard for truncating NP in the PIMC method is for the result to stabilize, the calculation time of PIMC is relatively long, especially in the case without the tumor where the paths keep walking before truncation. It should be noted that the results in Fig. 11 and Fig. 12 are obtained by polynomial interpolation of the PIMC results only on a 3×3 mesh on each electrode.

The proposed method provides a very effective method to solve a single-point

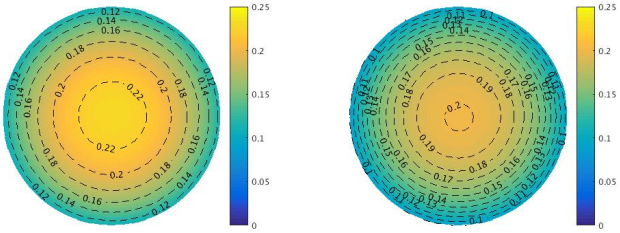

Fig. 11: Potentials on the north pole electrode by PIMC in case 1 (left: no tumor; right: with tumor)

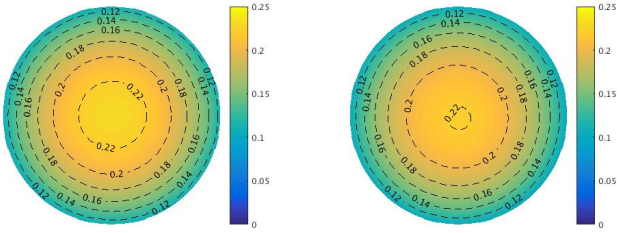

Fig. 12: Potentials on the north pole electrode by PIMC in case 2 (left: no tumor; right: with tumor)

problem in field analysis. Correspondingly, if BEM is used to solve the single-point problem, it is necessary to build a global mesh and solve a large global matrix. If only potentials at several points such as the center of each electrode are needed, the time cost used by the PIMC method will be much smaller than that required by the BEM. The proposed PIMC method also has a huge advantage in that the simulation of each path from each point is independent, and the storage space used is very minimal, which means that the algorithm can easily achieve a good parallel efficiency.

In addition, in our calculations, the contact impedance z_l is taken to be 0.5 while it can be very close to zero in practice. In that case, the voltages will jump drastically and then a denser mesh for the BEM must be required at the contacts to avoid large errors in the voltages. On the other hand, the PIMC will not be affected as each point is independently calculated.

Finally, in terms of the difficulty of programming, the code implementation of the proposed PIMC method is straightforward. Compared with a large amount of matrix entry calculation in the BEM method, the implementation of the WOS method is much simpler and not prone to coding errors. When the geometry of the domain in 3-D is complicated or boundary integral equation is difficult to solve, the PIMC method will be a preferred method to use.

6. Conclusions and future work. This paper presents a path integral Monte Carlo method to solve the forward problem of EIT and the voltage-to-current map for iterative algorithms of the inverse EIT problem where a forward problem needs

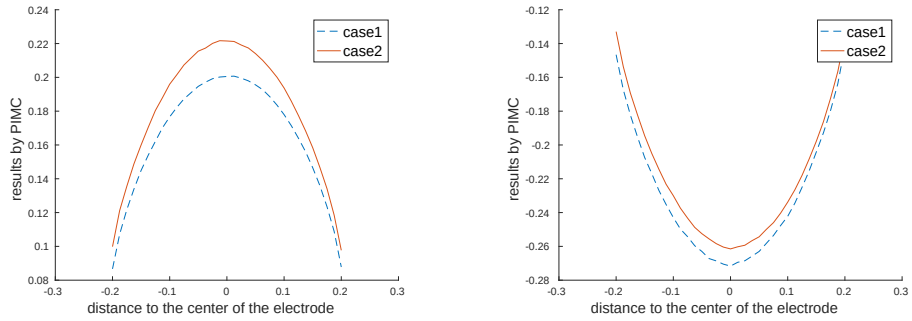

(a) Potentials on E_0 (with tumor). (b) Potentials on E_1 (with tumor).

Fig. 13: Potentials along the equator on the electrodes.

Table 8: Computational time cost (BEM)

	equation size	*time*$(s)^1$	*time*$(s)^2$	*total time*(s)	*average time per mesh point*(s)
no tumor	77388	29062	6625	35687	0.46
with tumor (*case* 1)	80330	28620	46717	75337	0.94
with tumor (*case* 2)	80330	28767	45484	74251	0.92

[1] the time for building the boundary integral equation.
[2] the time for solving the boundary integral equation.

to be solved at each iteration. The method is intrinsically parallel and potentials and currents can be calculated simultaneously at different electrodes, independently. The ill-posedness of the inverse problem requires high accuracy of the forward solver, otherwise it may lead to large errors in the reconstruction of conductivity. The PIMC method is accurate enough and is preferred over traditional boundary element or finite element methods when solution only on the electrodes are needed.

In a broader sense, the PIMC method can give single-point field analysis problem with the mixed boundary conditions. Solving the single-point problem directly and quickly is an advantage of the method over global deterministic algorithms. Moreover, the PIMC method is not only suitable for electric field analysis, but also for other field analysis problems, which will be considered for future work. To further improve the efficiency of the PIMC method, importance sampling of paths will also be investigated by using a prior estimate of the hitting probability of the Brownian paths in terms of the location and geometry of the boundary [29].

Acknowledgment. W.Cai thanks L. Borcea and E. Hsu for helpful discussions on the EIT and Feynman-Kac formulas, respectively, during this work.

REFERENCES

[1] M. Cheney, Margaret, D. Isaacson, and Jonathan C. Newell., *Electrical impedance tomography*, SIAM review 41, no. 1 (1999): 85-101.
[2] L. Borcea, Electrical impedance tomography, Inverse problems 18.6 (2002): R99.
[3] G. Alessandrini, *Stable determination of conductivity by boundary measurements*, Applicable

Analysis 27.1-3 (1988): 153-172.
[4] R. Kohn and M. Vogelius, *Determining conductivity by boundary measurements*, Comm. Pure Appl. Math., 37 (1984), pp. 113-123.
[5] J. Sylvester and G. Uhlmann, *A uniqueness theorem for an inverse boundary value problem in electrical prospection*, Comm. Pure Appl. Math., 39 (1986), pp. 91-112.
[6] A. P. Calderón, *On an inverse boundary value problem*, Computational & Applied Mathematics 25.2-3 (2006): 133-138.
[7] F. Santosa, M. Vogelius *A backprojection algorithm for electrical impedance imaging*, SIAM Journal on Applied Mathematics, (1990)216-43.
[8] J. P. Kaipio, et al, *Statistical inversion and Monte Carlo sampling methods in electrical impedance tomography*, Inverse problems 16.5 (2000): 1487.
[9] M. Vauhkonen et al., *Tikhonov regularization and prior information in electrical impedance tomography*, IEEE transactions on medical imaging 17.2 (1998): 285-293.
[10] A. Borsic, B. M. Graham, A. Adler, and W. RB Lionheart, *Total variation regularization in electrical impedance tomography*, (2007).
[11] S. Maire and M. Simon, *A partially reflecting random walk on spheres algorithm for electrical impedance tomography*, Journal of Computational Physics 303 (2015): 413-430.
[12] K.K. Sabelfeld, D. Talay, Integral formulation of the boundary value problems and the method of random walk on spheres, Monte Carlo Methods Appl. 1 (1995) 1-34.
[13] E. Somersalo, M. Cheney, and D. Isaacson, *Existence and uniqueness for electrode models for electric current computed tomography*, SIAM J. on Appl. Math. 52.4 (1992): 1023-1040.
[14] Y. Zhou, W. Cai and (Elton) P. Hsu, *Computation of Local Time of Reflecting Brownian Motion and Probabilistic Representation of the Neumann Problem*, Commun. Math. Sci., Vol. 15(2017), 237-259.
[15] Y. Zhou, and W. Cai., *Numerical Solution of the Robin Problem of Laplace Equations with a Feynman-Kac Formula and Reflecting Brownian Motions*, Journal of Scientific Computing 69.1 (2016): 107-121.
[16] A.V. Skorokhod, *Stochastic equations for diffusion processes in a bounded region*, Theory of Probability & Its Applications 6.3 (1961), 264-274.
[17] (Elton) P. Hsu, *"Reflecting Brownian motion, boundary local time and the Neumann problem"*, Dissertation Abstracts International Part B: Science and Engineering[DISS. ABST. INT. PT. B- SCI. ENG.], Vol. 45, No. 6, 1984.
[18] H. Tanaka, *Stochastic differential equations with reflecting boundary condition in convex regions*, Hiroshima Mathematical Journal 9.1 (1979), 163-177.
[19] P.L. Lions and A.S. Sznitman, *Stochastic differential equations with reflecting boundary conditions*, Communications on Pure and Applied Mathematics 37.4 (1984), 511-537.
[20] P. Lévy, *Processus Stochastiques et Mouvement Brownien, Gauthier-Villars*, Paris, 1948.
[21] I. Karatzas and S. E. Shreve, *Brownian motion and stochastic calculus*, Springer-Verlag New York Inc., 1988.
[22] J.F. Douglas, *Integral equation approach to condensed matter relaxation*, Journal of Physics: Condensed Matter 11.10A (1999), A329.
[23] M. E. Müller, *Some continuous Monte Carlo methods for the Dirichlet problem*, The Annals of Mathematical Statistics, Vol. 27, No. 3, 569-589, 1956.
[24] K. L. Chung, *Green, Brown, and Probability and Brownian Motion on the Line*, World Scientific Pub Co Inc, 2002.
[25] J. A. Given, C. Hwang and M. Mascagni, *First-and last-passage Monte Carlo algorithms for the charge density distribution on a conducting surface*, Phys. Rev. E 66, 056704, 2002.
[26] V. G. Papanicolaou, The probabilistic solution of the third boundary value problem for second order elliptic equations, Probab. Th. Rel. Fields 87 (1990), 27-77.
[27] J. P. Morillon, *Numerical solutions of linear mixed boundary value problems using stochastic representations*, Int. J. Numer. Meth. Engng., Vol. 40, 387-405, 1997.
[28] H.M. Lin, H.Z. Tang, and W. Cai, *Accuracy and efficiency in computing electrostatic potential for an ion channel model in layered dielectric/electrolyte media*, Journal of Computational Physics 259 (2014): 488-512.
[29] Z. Schuss, Brownian dynamics at boundaries and interfaces. Springer-Verlag New York; 2015.